

Article

Apparent Resistivity Variation Imaging Method Based on Magnetic Field Gradient by NGO-LSSVM for the Ground-Airborne Frequency-Domain Electromagnetic Method

Changsheng Liu ^{1,2}, Jie Liang ^{1,2}, Shuxu Liu ^{1,2}  and Haigen Zhou ^{1,2,*} 

¹ College of Instrumentation and Electrical Engineering, Jilin University, Changchun 130021, China; liuchangsheng@jlu.edu.cn (C.L.); liangjie19@mails.jlu.edu.cn (J.L.); sxliu22@mails.jlu.edu.cn (S.L.)

² Key Laboratory of Geophysical Exploration Equipment, Ministry of Education, Jilin University, Changchun 130021, China

* Correspondence: zhouhaigen@jlu.edu.cn

Abstract: Apparent resistivity imaging is a typical rapid imaging method in the ground-airborne frequency-domain electromagnetic method. At present, the apparent resistivity is typically calculated by the measured magnetic field, however, this imaging method exhibits limited capability in recognizing the center of three-dimensional anomalies. Therefore, this paper proposed the calculation of apparent resistivity using magnetic field gradients. To solve the problem of random artificial anomalies that existed during the calculated process, this paper presents a hybrid least square support vector machine (LSSVM) and Northern Goshawk optimization (NGO) to establish the mapping relationship between the magnetic field gradient and apparent resistivity variation. This approach enables accurate prediction of apparent resistivity variations and effectively resolves the challenge of correcting background resistivity. Furthermore, three typical theoretical models and field examples are used to predict the apparent resistivity variation, the imaging results demonstrate that the proposed NGO-LSSVM algorithm is a feasible and efficient tool for predicting the apparent resistivity variation with high accuracy. This study provides a novel and efficient imaging method, which facilitates the application of ground-airborne frequency-domain electromagnetics for high-resolution detection requirements, such as mineral exploration.

Keywords: magnetic field gradient; apparent resistivity variation imaging; NGO-LSSVM; ground-airborne frequency-domain electromagnetic; high-resolution electromagnetic detection tools



Citation: Liu, C.; Liang, J.; Liu, S.; Zhou, H. Apparent Resistivity Variation Imaging Method Based on Magnetic Field Gradient by NGO-LSSVM for the Ground-Airborne Frequency-Domain Electromagnetic Method. *Appl. Sci.* **2024**, *14*, 3569. <https://doi.org/10.3390/app14093569>

Academic Editor: Adel Razek

Received: 27 March 2024

Revised: 20 April 2024

Accepted: 21 April 2024

Published: 24 April 2024



Copyright: © 2024 by the authors. Licensee MDPI, Basel, Switzerland. This article is an open access article distributed under the terms and conditions of the Creative Commons Attribution (CC BY) license (<https://creativecommons.org/licenses/by/4.0/>).

1. Introduction

Ground-airborne frequency-domain electromagnetic method (GAFEM) is one of the important geophysical exploration methods, which has high efficiency and is especially suitable for geological surveys under complex terrain conditions [1–4]. In frequency-domain electromagnetic interpretation, the received electromagnetic response is typically transformed into apparent resistivity, apparent depth, and other parameters that can characterize the subsurface electrical distribution. This enables the generation of visual cross-sectional images depicting the electrical properties of the subsurface medium and provides a foundation for subsequent interpretation work [2,5].

At present, the definition of the apparent resistivity in GAFEM is based on electromagnetic fields generated by a horizontal electric field source on the surface of a homogeneous half-space, and it only requires the z-component of the magnetic field [2]. Based on the monotonic relationship between the z-component magnetic field and resistivity, an iteration-matching procedure to calculate the apparent resistivity, based on the quasistatic response for a homogeneous half-space, was developed. Currently, the calculation of apparent resistivity involves magnetic fields. However, the magnetic field is sensitive to the interface where the resistivity varies, so the recognition resolution of the magnetic field is ideal

for one-dimensional objects, but limited for three-dimensional objects. To enhance the resolution of targets, Plessix et al. inverse the Hessian estimated by the BFGS method and realize a significant improvement of the inversion convergence and inversion results. It reduces the number of iterations by 2 to 4, but still needs 50 iterations [6]. Liu et al. present an improved CG algorithm that needs fewer iterations. However, the method has poor imaging ability for multiple object cases [7]. Qin et al. propose a full magnetic gradient orthonormal basis function method to effectively characterize magnetic anomaly of magnetic targets, and the SNR of the method is improved greatly. However, seven orthonormal functions are required to realize the method, which is tedious [8]. Liu's research demonstrates that the magnetic field gradient is more sensitive to the center of three-dimensional objects, thereby enhancing the recognition resolution, and realizing rapid imaging of space magnetic gradient anomaly [9]. Nevertheless, there is a lack of information regarding the calculation of the apparent resistivity derived from the magnetic field gradients. In this study, we investigate a conversion method for converting the apparent resistivity from magnetic field gradients, and compare it with the apparent resistivity calculated directly from the magnetic field.

Due to the monotonic relationship between the magnetic field gradient and underground resistivity, the iteration-matching procedure can be utilized for calculating apparent resistivity theoretically. However, the calculated apparent resistivity by the electromagnetic field gradient of the uniform earth has a background value [10], which needs to be corrected to avoid introducing false anomalies and affecting the resolution of anomalous objects. Since the background apparent resistivity is closely related to the background resistivity of the model, it is difficult to obtain the background apparent resistivity when solving an unknown model. Therefore, it is essential to establish a correlation between the magnetic field gradient and the apparent resistivity after correcting, i.e., apparent resistivity variation. In GAFEM, the relationship between resistivity and magnetic field response is implicit, so the iteration-matching algorithm is predominantly employed for the translation process [2]. The magnetic field undergoes a gradient calculation to derive the magnetic field gradient, which exhibits a more implicit relationship with resistivity variation. Consequently, the iterative process of converting the magnetic field gradient to apparent resistivity variation becomes more complex. The advancement of computer algorithms and the widespread use of machine learning has provided new approaches to the solution process [11–13].

Machine learning (ML) fits a certain non-linear mapping relationship based on big data, thereby avoiding the challenges associated with data analysis and mathematical modeling encountered in traditional mathematical-physical methods during data processing. Hence, ML offers distinct advantages for solving non-linear and complex problems [14,15]. In geophysical exploration, most geological models are characterized by non-linearities, so machine learning has been widely used in geophysical data processing and interpretation, such as lithology identification, curve fitting, and geophysical inversion, due to their unique non-linear fitting ability [16–19]. Support vector machine (SVM) is a classical machine learning method with a solid theoretical foundation and strong generalization performance [20]. Compared to deep neural networks, SVM requires fewer training samples, resulting in lower computing costs [21]. Many researchers have successfully applied SVM to geophysical data processing [22–24]. LSSVMs (least square support vector machines) are an extension of SVM that offers superior approximations for non-linear problems, making them a valuable tool for modeling and forecasting non-linear systems [25,26]. It requires fewer parameters and faster convergence to the optimal solution. However, the effectiveness of predictions heavily relies on the selection of kernel function parameters and regularization parameters. Therefore, when employing an LSSVM in computational optimization, careful consideration must be given to choosing the appropriate type of kernel function, as well as determining suitable values for its associated parameters. Generally, the Gaussian kernel function exhibits excellent anti-interference ability and is widely adopted. However, it is highly sensitive to parameter values which makes it necessary to optimize parameters when utilizing the Gaussian function. In this paper, the Gaussian kernel func-

tion is adopted to analyze the problem. Due to the parametric sensitivity of Gaussian kernel functions, it may not be appropriate to select parameters based on common experience. Therefore, an optimization algorithm is needed to optimize the two main parameters of the Gaussian kernel function, the kernel parameter, and the regularization parameter [27–29]. NGO (Northern Goshawk optimization) is a metaheuristic optimization algorithm designed for global optimization, which efficiently explores solution spaces [30–33].

Considering the non-linear relationship between the magnetic field gradient and apparent resistivity variation, this paper introduces NGO-LSSVM in apparent resistivity variation imaging for GAFEM, where NGO optimizes LSSVM parameters. First, the basic electromagnetic theory of magnetic field gradient response was studied to determine the characteristic parameters that affect apparent resistivity variation calculation. On this basis, the basic theory of LSSVM models and NGO algorithms was studied, and an optimized NGO-LSSVM model was developed. Finally, the prediction effect of the NGO-LSSVM model was verified by predicting the apparent resistivity variation of the theoretical models and field data.

2. Theory and Methodology

2.1. Apparent Resistivity Calculated by the Magnetic Field Gradient

The schematic diagram of GAFEM detection system is shown in Figure 1; the electric source is located in the origin along the x -axis, and the z -axis is positive downward, with the origin at the center of the electric source. The received magnetic sensor is in the air, lifted by an unmanned aerial vehicle, (x_r, y_r, z_r) is the coordinate of the receiver point.

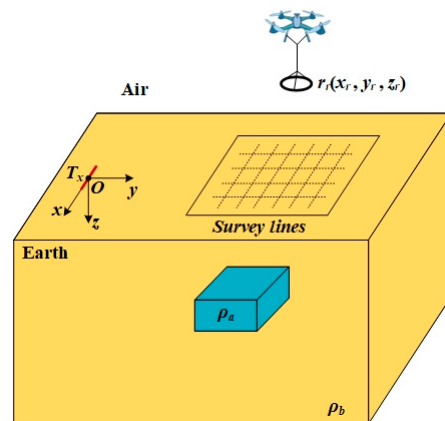


Figure 1. Schematic diagram of ground-airborne electromagnetic detection.

The FEM response of the magnetic field response H_z of the receiver point in a uniform half-space can be expressed as [2]

$$\begin{aligned}
 H_z &= \frac{IL}{2\pi} \cdot \frac{y_r}{R} \int_0^\infty \frac{\lambda^2}{\lambda + u_1} e^{\lambda z_r} J_1(\lambda R) d\lambda \\
 &= \frac{-3iILy_r\rho}{2\pi\omega\mu R^3} [1 - e^{-ik_1 R} (1 + ik_1 R - \frac{1}{3}k_1^2 R^2)],
 \end{aligned}
 \tag{1}$$

where $R = (x_r^2 + y_r^2 + z_r^2)^{1/2}$, J_1 is the first-order Bessel function, $u_1 = (\lambda^2 - k_1^2)^{1/2}$, $k_1^2 = \omega^2\mu\varepsilon - i\omega\mu\sigma$, f is the transmitting frequency, the angular frequency $\omega = 2\pi f$ is sufficiently low that displacement currents are negligible, i.e., $k_1^2 = -i\omega\mu\sigma$, λ is the Hankel integral variable, ρ is the resistivity of the earth, $\sigma = 1/\rho$, μ , and ε are the conductivity, magnetic permeability, and electric permittivity of the earth, respectively. IL is the transmitting electric moment, i is the imaginary unit.

According to Liu et al. [9], the space magnetic gradient anomaly can recognize the underground electrical anomalies effectively, the spatial gradient of H_z at the receiver point can be calculated by:

$$H_z^{\Delta x}(x_i, y_j, z_k, f) = \frac{|H_z(x_i, y_j, z_k, f)| - |H_z(x_{i-1}, y_j, z_k, f)|}{\Delta L_x}, \tag{2}$$

$$H_z^{\Delta y}(x_i, y_j, z_k, f) = \frac{|H_z(x_i, y_j, z_k, f)| - |H_z(x_i, y_{j-1}, z_k, f)|}{\Delta L_y}. \tag{3}$$

where $\Delta L_x = |x_i - x_{i-1}|$ and $\Delta L_y = |y_j - y_{j-1}|$ represents the distance between the two adjacent points in the x direction and y direction, respectively. Subscripts i, j, k represent the number of the receiver point coordinates in x, y, z direction, respectively. Equations (1)–(3) reveal that the primary influencing factors of the magnetic field gradient include the coordinates of the receiver point, transmitting frequency, and subsurface electric parameter ρ . To investigate the relationship between the magnetic field gradient and the resistivity, we calculate the magnetic field gradient for a changing resistivity of the homogeneous earth as an example, the receiver point and transmitting frequency are set as (3000, 5000, -30) m, $f = 64$ Hz, as shown in Figure 2.

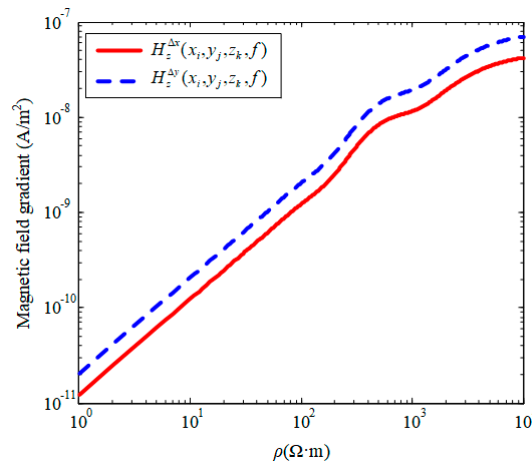


Figure 2. Relationship between the magnetic field gradients and resistivity.

As shown in Figure 2, as the resistivity increases, both the magnetic gradients in the x and y directions exhibit a consistent upward trend, i.e., at a certain observation point, there exists a one-to-one mapping relationship between the magnetic field gradient and resistivity. Due to the implicit relationship between the magnetic field gradient and resistivity, Equations (2) and (3) are equations with unknown resistivity, not a solution to the equation. Therefore, the optimal value of apparent resistivity can be obtained by solving Equations (2) and (3) using the iteration-matching algorithm. For a known value $H_z^{\Delta x}$ or $H_z^{\Delta y}$ at a given survey point and a given frequency, an initial range of resistivity value is provided, and the resistivity ρ is iteratively calculated using the bisection method until the error between the calculated and known magnetic field gradients is less than a predefined threshold (e.g., 1%). The resulting resistivity value at this point represents the optimal apparent resistivity.

Figure 3 is the apparent resistivity solved from magnetic field gradient of uniform half-space models with various resistivity values. Model parameters are $\rho = 10, 100,$ and $1000 \Omega\cdot\text{m}$, respectively; the transmitting frequency range is set from 16 Hz to 8192 Hz.

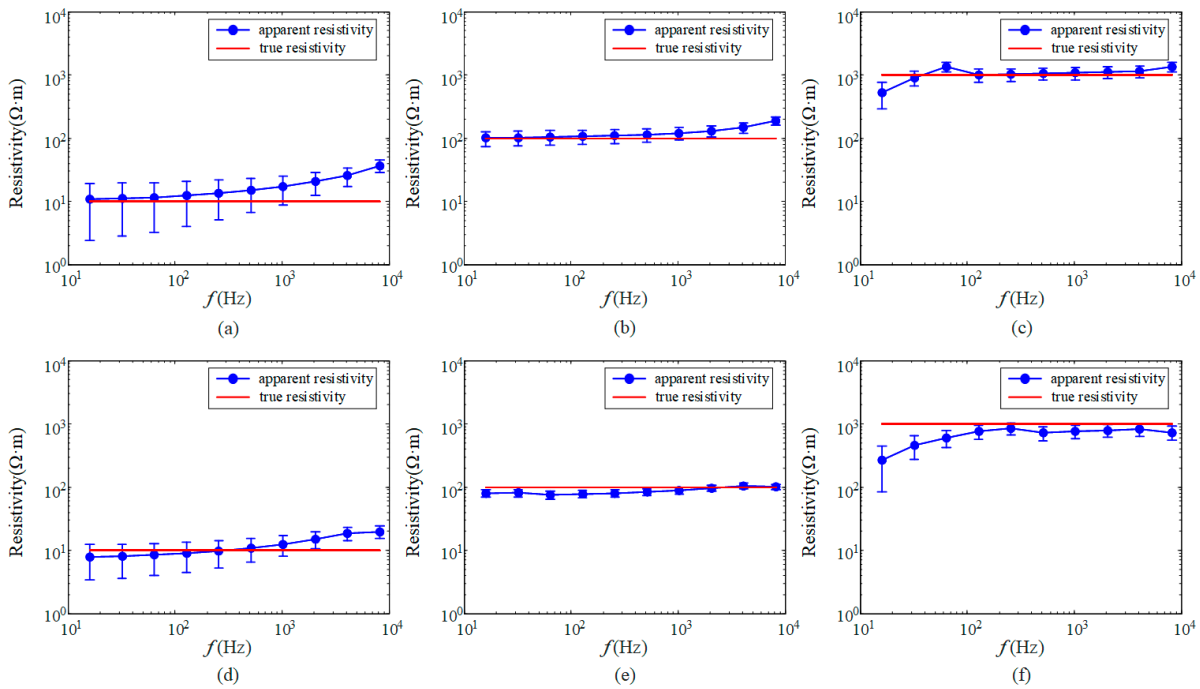


Figure 3. Calculated apparent resistivities from (a–c) x -direction magnetic field gradient $H_z^{\Delta x}$; (d–f) y -direction magnetic field gradient $H_z^{\Delta y}$ of uniform half-space models with different resistivities.

Figure 3a–c shows the calculated apparent resistivity from $H_z^{\Delta x}$ by Equation (2), Figure 3d–f shows the calculated apparent resistivity from $H_z^{\Delta y}$ by Equation (3). Globally, the calculated apparent resistivity distributes near the true model, but there are varying calculation errors for different models. Specifically, in Figure 3a,d, when the uniform earth resistivity is $10 \Omega \cdot m$, the apparent resistivity in the high-frequency band significantly deviates from the true model, and when the frequency is 8192 Hz , the deviation reaches a maximum of $26 \Omega \cdot m$. In Figure 3b,e, when the earth resistivity is $100 \Omega \cdot m$, there exists a larger error in calculating apparent resistivity using the x -direction gradient $H_z^{\Delta x}$ in the high-frequency band, the deviation reaches a maximum of $87 \Omega \cdot m$ when $f = 8192 \text{ Hz}$; while the y -direction gradient $H_z^{\Delta y}$ yields a larger error in the low-frequency band, the deviation reaches a maximum of $24 \Omega \cdot m$ when $f = 64 \text{ Hz}$. In Figure 3c,f, when the earth resistivity is $1000 \Omega \cdot m$, there is a distinct difference between the calculated apparent resistivity and real model in the low-frequency band, when the frequency is 16 Hz , the deviation reaches a maximum of $732 \Omega \cdot m$. The irregular calculation errors of the uniform model may result in random artificial anomalies in apparent resistivity imaging of anomaly models. Therefore, this deviation cannot be ignored.

In order to mitigate the presence of random artificial anomalies, for the anomaly models, it is necessary to eliminate the non-uniform apparent resistivity derived from the uniform earth model. The difference between the apparent resistivity calculated from the anomaly model and that from the background uniform model is defined as the apparent resistivity variation $\Delta\rho$. Generally, the background resistivity remains unknown during detection. Therefore, this study employs LSSVM to obtain the apparent resistivity variation eliminating the background resistivity of the uniform model when its value is unknown. The inputs include the geometric position of measurement points, the transmitting frequency, and magnetic field gradient values. For correcting background apparent resistivity, we utilize the apparent resistivity variation as output to train our network.

2.2. Least Square Support Vector Machines

LSSVM inherits the generalization capability and robustness of SVM, with the added benefit of superior computational efficiency compared to SVM. LSSVM transforms the

inequality constraints of SVM into equations, adds an error variable, and introduces the L2 regularization term of the error variable as a penalty term, which improves the accuracy and speed of convergence. In this paper, we consider a given sample dataset $\{x_k, y_k\}_{k=1}^N$, where x_k denotes the input data, y_k denotes the target data, N is the total number of samples. In the feature space, the regression function can be given by [25,26]

$$y(x) = w^T \phi(x) + b, \tag{4}$$

where w is the weight vector, b is the bias term, $\phi(x)$ is the non-linear function that maps the input data points to a high-dimensional feature space where linear regression is performed.

According to the structural risk minimization principle, the objective function and constraints can be described as:

$$\begin{aligned} \min_{w,b,e} J(w, \zeta) &= \frac{1}{2} w^T w + \frac{1}{2} \gamma \sum_{k=1}^N \zeta_k^2 \\ \text{s.t. } y_k &= w^T \phi(x_k) + b + \zeta_k, \quad k = 1, 2, \dots, N, \end{aligned} \tag{5}$$

where γ is a regularization parameter, ζ_k is the slack variable.

Using the Lagrange method to solve the optimization problem, it follows that

$$L(w, b, \zeta, \alpha) = \frac{1}{2} w^T w + \frac{1}{2} \gamma \sum_{k=1}^N \zeta_k^2 - \sum_{k=1}^N \alpha_k \{w^T \phi(x_k) + b + \zeta_k - y_k\}, \tag{6}$$

where α_k is the Lagrange multiplier. The conditions for optimality can be obtained by differentiating with respect to the primal variables w, b, ζ_k , and α_k ,

$$\begin{aligned} \frac{dL}{dw} = 0 &\rightarrow w = \sum_{k=1}^N \alpha_k \phi(x_k), \\ \frac{dL}{db} = 0 &\rightarrow \sum_{k=1}^N \alpha_k = 0, \\ \frac{dL}{d\zeta_k} = 0 &\rightarrow \alpha_k = \gamma \zeta_k, \quad k = 1, 2, \dots, N, \\ \frac{dL}{d\alpha_k} = 0 &\rightarrow y_k = w^T \phi(x_k) + b + \zeta_k, \quad k = 1, 2, \dots, N, \end{aligned} \tag{7}$$

By elimination of w and ζ_k , the linear system can be obtained as follows [34]:

$$\begin{bmatrix} 0 & 1 & \dots & 1 \\ 1 & K(x, x_k) + \gamma^{-1} & \dots & K(x, x_k) \\ \vdots & \vdots & \dots & \vdots \\ 1 & K(x, x_k) & \dots & K(x, x_k) + \gamma^{-1} \end{bmatrix} \begin{bmatrix} b \\ \alpha_1 \\ \vdots \\ \alpha_N \end{bmatrix} = \begin{bmatrix} 0 \\ y_1 \\ \vdots \\ y_N \end{bmatrix}, \tag{8}$$

where the kernel function $K(x, x_k) = \phi(x_k)^T \phi(x)$ is a symmetric function satisfying the conditions of Mercer's theorem [35]. The resulting LSSVM for the function estimation can thus be formulated as

$$y(x) = \sum_{k=1}^N \alpha_k K(x, x_k) + b, \tag{9}$$

The LSSVMs employ various kernel functions, including linear kernel functions, polynomial kernel functions, radial basis functions (RBFs), and sigmoid kernel functions. The radial basis function, which has fewer parameters and a strong generalization ability, is adopted and its expression is as follows:

$$K(x, x_k) = \exp\left(-\frac{\|x - x_k\|^2}{2\sigma^2}\right). \tag{10}$$

where σ is the width of the radial basis function.

The optimization problem of the LSSVM parameters is commonly transformed into a parametric estimation problem of a multiple linear regression function. The regularization parameter γ and the kernel parameter σ significantly impact the performance of the LSSVM model, so optimizing them is necessary to prevent poor accuracy caused by random parameters and premature convergence to locally optimal solutions.

2.3. Northern Goshawk Optimization

To obtain the optimal values of the regularization parameter γ and the kernel parameter σ in LSSVM, the NGO algorithm proposed by Dehghani M is employed to optimize the parameters in this paper [30]. The NGO algorithm is a population-based algorithm that incorporates an efficient search and capture mechanism inspired by prey behavior. Therefore, the algorithm consists of three phases: population initialization, prey identification, and prey capture.

2.3.1. Initialization

At the beginning of the algorithm, individuals within the population are initialized randomly across the search space, the population matrix X can be expressed as:

$$X = \begin{bmatrix} X_1 \\ \vdots \\ X_i \\ \vdots \\ X_N \end{bmatrix}_{N \times m} = \begin{bmatrix} x_{1,1} & \dots & x_{1,j} & \dots & x_{1,m} \\ \vdots & \ddots & \vdots & \ddots & \vdots \\ x_{i,1} & \dots & x_{i,j} & \dots & x_{i,m} \\ \vdots & \ddots & \vdots & \ddots & \vdots \\ x_{N,1} & \dots & x_{N,j} & \dots & x_{N,m} \end{bmatrix}_{N \times m} \quad (11)$$

where X represents the population of northern goshawks, X_i denotes the i th proposed solution, $x_{i,j}$ signifies the value of the j th variable specified by the i th proposed solution, N is the number of population members, and m is the number of problem variables.

The objective function value is calculated by Equation (12).

$$F(X) = \begin{bmatrix} F_1 = F(X_1) \\ \vdots \\ F_i = F(X_i) \\ \vdots \\ F_N = F(X_N) \end{bmatrix}_{N \times 1} \quad (12)$$

where vector F is the obtained objective function values, F_i is the objective function value acquired from i th proposed solution.

2.3.2. Prey Identification

The Northern Goshawk randomly selects a prey to achieve a global search. The main process is represented by Equations (13)–(15).

$$P_i = X_k, i = 1, 2, \dots, N, k = 1, 2, \dots, i - 1, i + 1, \dots, N \quad (13)$$

$$x_{i,j}^{new,P1} = \begin{cases} x_{i,j} + r(p_{i,j} - Ix_{i,j}), & F_{P_i} < F_i \\ x_{i,j} + r(x_{i,j} - p_{i,j}), & F_{P_i} \geq F_i \end{cases} \quad (14)$$

$$X_i = \begin{cases} X_i^{new,P1}, & F_i^{new,P1} < F_i \\ X_i, & F_i^{new,P1} \geq F_i \end{cases} \quad (15)$$

where P_i represents the prey position for the i th Northern Goshawk, F_{P_i} denotes its objective function value, k is a random natural number, $X_i^{new,P1}$ signifies the new status for the i th proposed solution, $x_{i,j}^{new,P1}$ refers to its j th dimension, $F_i^{new,P1}$ indicates its objective function

value based on the first phase of NGO, r is a random number within the interval $[0, 1]$, and I is a random number that can take values 1 or 2. Parameters r and I are utilized to introduce a random behavior in the search and update processes of NGO.

2.3.3. Chase and Escape Operation

Suppose the hunting is close to an attack position with radius R , the main process is represented by Equations (16)–(18):

$$x_{i,j}^{new,P2} = x_{i,j} + R(2r - 1)x_{i,j} \tag{16}$$

$$R = 0.02 \left(1 - \frac{t}{T} \right) \tag{17}$$

$$X_i = \begin{cases} X_i^{new,P2}, & F_i^{new,P2} < F_i \\ X_i, & F_i^{new,P2} \geq F_i \end{cases} \tag{18}$$

where t represents the iteration counter, T denotes the maximum number of iterations, $X_i^{new,P2}$ signifies the updated status for i th proposed solution, $x_{i,j}^{new,P2}$ refers to its j th dimension, $F_i^{new,P2}$ indicates its objective function value based on the second phase of NGO.

2.4. Analysis of Simulation Results

We adopt uniform earth models with different resistivity and abnormal models with different parameters to obtain the magnetic field gradient data through forward calculation. Firstly, we calculated the apparent resistivity through the bisection method by solving Equations (2) and (3), and then corrected its background resistivity to obtain the corresponding apparent resistivity variation as the output variable, and constructed a dataset for training. In this paper, the number of populations in the NGO algorithm is set to 20 and the number of iterations is 50. The iterative convergence curve of the NGO in the prediction model NGO-LSSVM is shown in Figure 4. From the iterative convergence curve, it can be seen that NGO reaches the optimal solution by the second iteration and then remains stable, which proves that the NGO algorithm converges quickly, and the results are stable. After the optimization of the NGO algorithm, the regularization parameter γ is finally determined to be 0.1, and the kernel parameter σ is 800. The two parameters are taken as the corresponding parameter values of LSSVM, that is, the optimization process of LSSVM is completed.

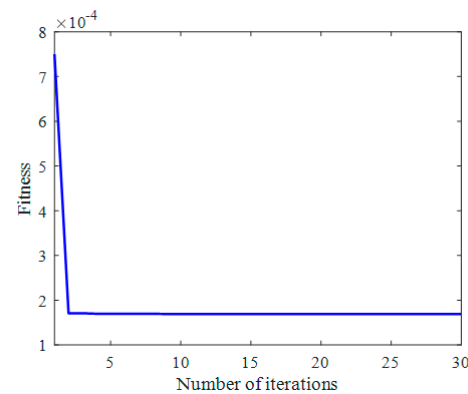


Figure 4. Fitness curve of the iterative process.

Figure 5 shows the prediction results of the NGO-LSSVM model. Figure 5a represents the partial prediction results of the training set, and Figure 5b is the prediction results of the test set. In both datasets, a strong consistency is observed between the predicted values and true values.

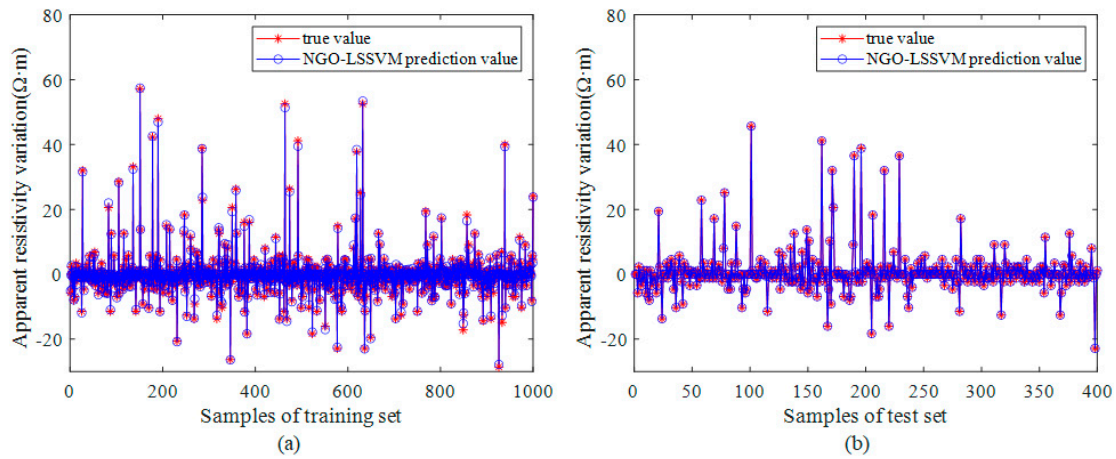


Figure 5. Partial prediction results of (a) training set and (b) test set.

To verify the correction of the background apparent resistivity by the NGO-LSSVM model, the predicted apparent resistivity variation of uniform half-space models in Figure 3 is shown in Figure 6. The results of Figure 6 reveal that regardless of whether the resistivity of a homogeneous earth is 10, 100, or 1000 Ω·m, as long as it remains uniform without any changes in resistivity, the apparent resistivity variation is zero. In other words, the apparent resistivity variation is not sensitive to the background resistivity and only reflects the change in the resistivity of the medium.

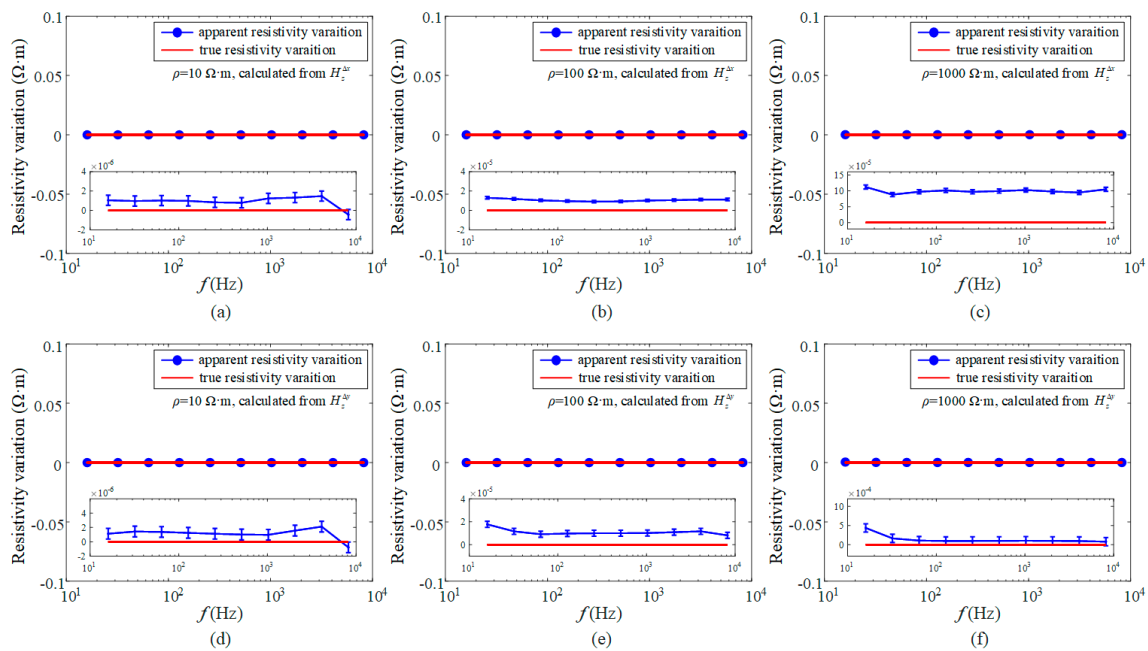


Figure 6. Predicted apparent resistivity variations by NGO-LSSVM algorithm from (a–c) x -direction magnetic field gradient $H_z^{\Delta x}$, (d–f) y -direction magnetic field gradient $H_z^{\Delta y}$ of uniform half-space models with different resistivities.

To compare the data before and after correction more intuitively, the errors of apparent resistivity and apparent resistivity variation are shown in Figure 7. In view of the strong correlation between the error of apparent resistivity and the true value of apparent resistivity, we calculated the relative error of apparent resistivity, as shown in Figure 7a. Due to the weak correlation between the error of apparent resistivity variation and the true value of apparent resistivity variation, the errors of predicted apparent resistivity variation are calculated, as shown in Figure 7b. It can be seen that the proposed prediction method of

apparent resistivity variation can significantly reduce the calculation error and improve the calculation accuracy.

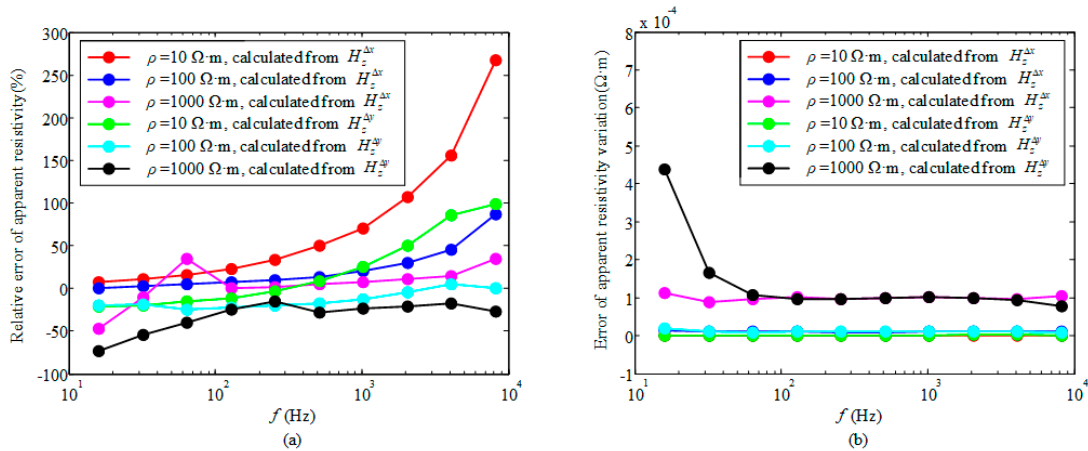


Figure 7. Error of apparent resistivity and apparent resistivity variation. (a) Relative error of the calculated apparent resistivity, (b) error of predicted apparent resistivity variation.

3. Theoretical Model Testing

To verify the predictive capability of the NGO-LSSVM algorithm for three-dimensional models, we designed experiments involving conductive targets embedded in a homogenous half-space. Model I is shown in Figure 8, the central point coordinate of the conductive target is (3000, 5000, 500) m, and the length of the conductive body is 400 m × 400 m × 200 m. The resistivity of the earth and the conductive target are set to 100 Ω·m and 10 Ω·m, respectively. To verify the imaging effect of the magnetic gradient in the *x*-direction and *y*-direction, respectively, two perpendicular survey lines are set above the conductive target, as the dotted lines shown in Figure 8.

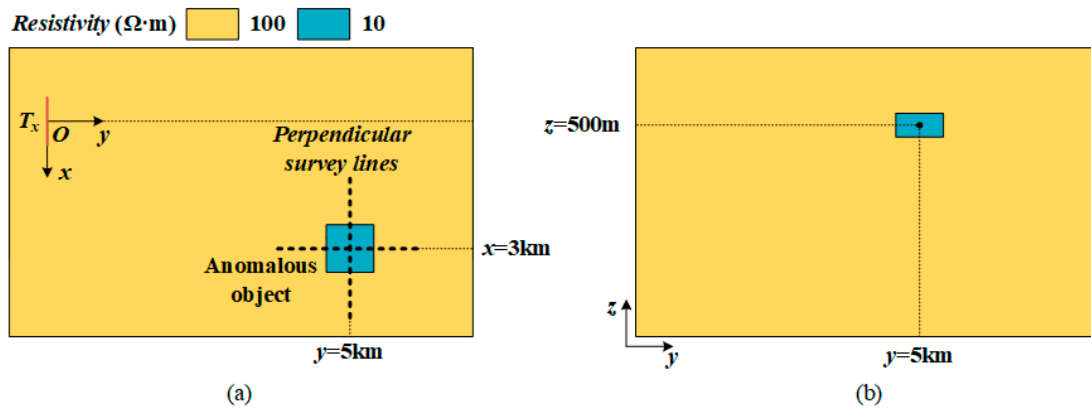


Figure 8. Schematic diagram of the model I with a conductive object: (a) XOY plane, (b) YOZ plane.

The apparent resistivity and apparent resistivity variation results are obtained using the traditional iteration-matching method and NGO-LSSVM algorithm respectively, as shown in Figure 9. The white box indicates the outline of the conductive abnormal body. In Figure 9a,c, a high resistance pole is observed at the left boundary of the object, while a low resistance pole exists at the right boundary. The changing range of the apparent resistivity shows a significant spread. In Figure 9b,d, both the apparent resistivity variation in the *x*-direction $\Delta\rho^{\Delta x}$ and *y*-direction $\Delta\rho^{\Delta y}$ obtain the pole at the center of the abnormal body, which can indicate the location of the abnormal body. Compared to the apparent resistivity, the apparent resistivity variations exhibit a more compact changing area.

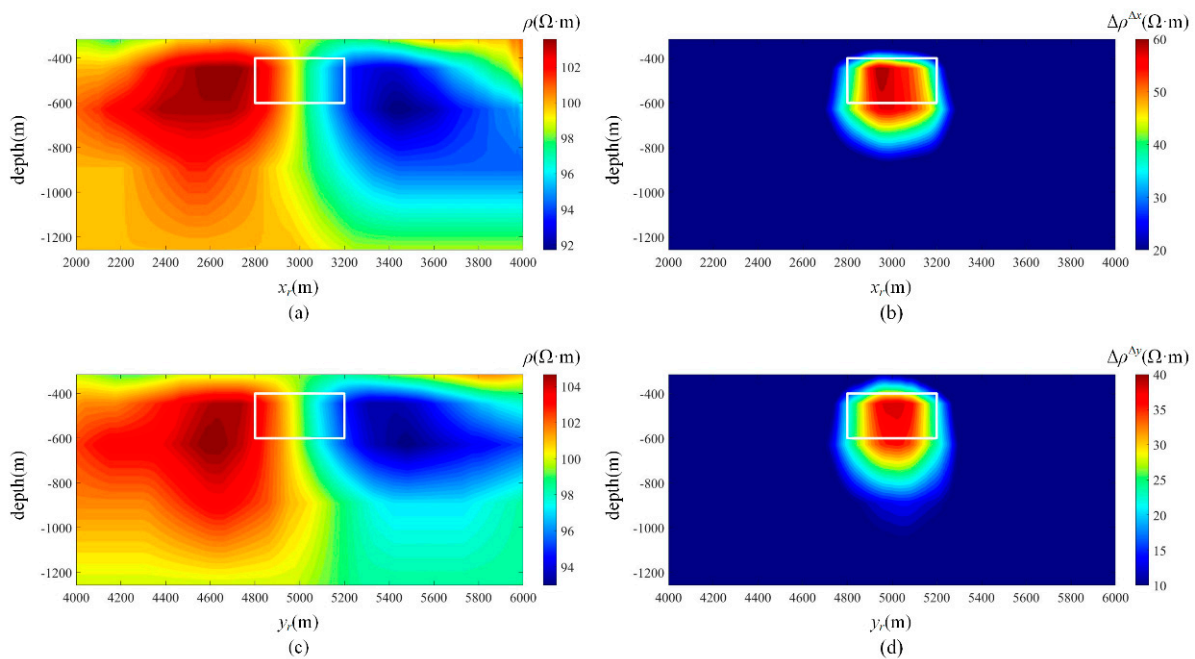


Figure 9. The imaging results for the model I: (a) the apparent resistivity calculated from magnetic field, (b) the apparent resistivity variation predicted from magnetic field gradient $H_z^{\Delta x}$ along the x -direction survey line, (c) the apparent resistivity calculated from magnetic field, (d) the apparent resistivity variation predicted from magnetic field gradient $H_z^{\Delta y}$ along the y -direction survey line. The white box indicates the outline of the conductive abnormal body.

To verify the universality of the proposed method, model II was established with two anomalous objects positioned along the x -axis, as shown in Figure 10. The central point coordinates of the two conductive targets are (2200, 5000, 500) m and (3000, 5000, 500) m, respectively. An x -direction survey line is set above the conductive targets, as the dotted line shown in Figure 10. The imaging results for model II are shown in Figure 11. Figure 11a exhibits the apparent resistivity calculated from the magnetic field H_z by the traditional bisection iteration method. For both anomalous bodies, the apparent resistivity on the left side is high and the apparent resistivity on the right side is low. Different from the single anomalous body model in Figure 8, there exists an apparent resistivity transition region between the highest and lowest values of apparent resistivity, precisely located in the middle of the two anomalous bodies. The transition region of apparent resistivity makes a gradual change in the distribution of apparent resistivity from near source to far source, exhibiting a monotonic decrease. The center of both anomalous bodies exhibits an apparent resistivity interface, indicating a significant change in apparent resistivity. Figure 11b exhibits the apparent resistivity variation predicted from magnetic field gradient $H_z^{\Delta x}$ by the NGO-LSSVM model. The center of the two anomalous bodies exhibits a maximum value of apparent resistivity variation, indicating a clear localization of the anomalous bodies.

The model III was established with two anomalous objects positioned along the y -axis, as shown in Figure 12. The central point coordinates of the two conductive targets are (3000, 4200, 500) m and (3000, 5000, 500) m, respectively. A y -direction survey line is set above the conductive targets, as the dotted line shown in Figure 12. The imaging results for model III are shown in Figure 13. Similar to the imaging pattern in Figure 11, the apparent resistivity in Figure 13 has the change interface positioned at the center of the two anomalous bodies. Additionally, the variation of apparent resistivity in the y -direction has clear traps at the center of the anomalous bodies.

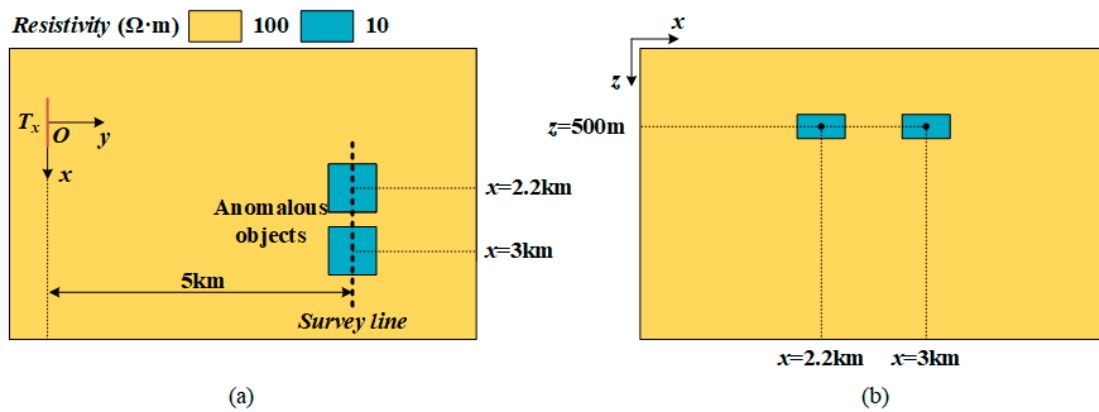


Figure 10. Schematic diagram of the model II with two conductive objects positioned along the x -axis: (a) XOY plane, (b) XOZ plane.

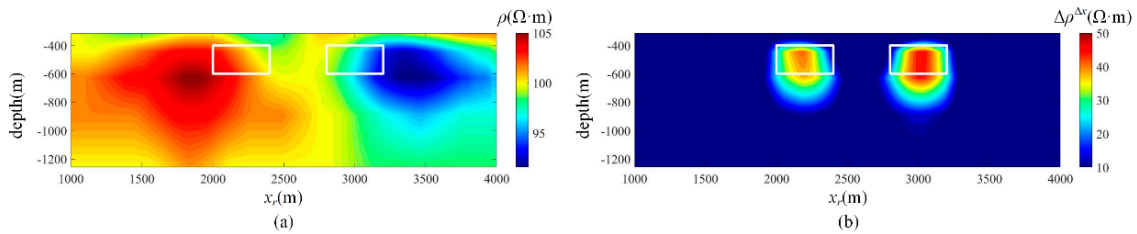


Figure 11. The imaging results for model II: (a) the apparent resistivity calculated from magnetic field, (b) the apparent resistivity variation predicted from magnetic field gradient $H_z^{\Delta x}$. The white boxes indicate the outlines of the conductive abnormal bodies.

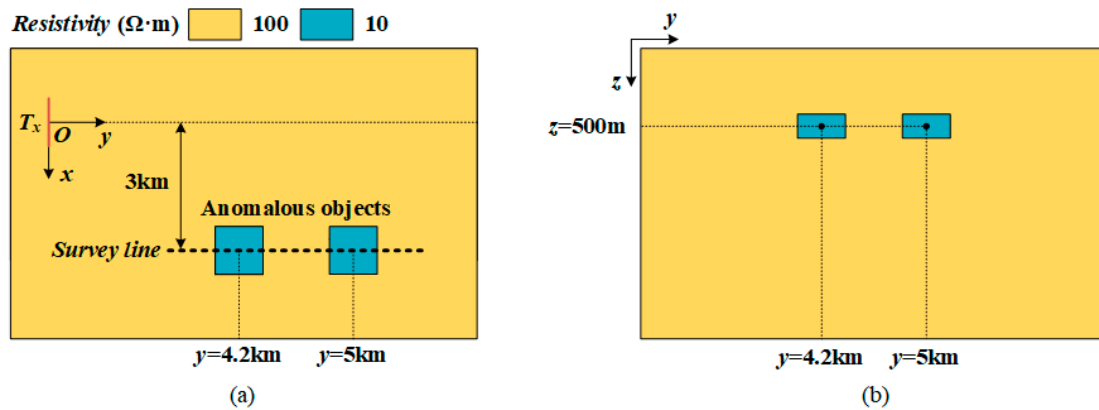


Figure 12. Schematic diagram of model III with two conductive objects positioned along the y -axis: (a) XOY plane, (b) YOZ plane.

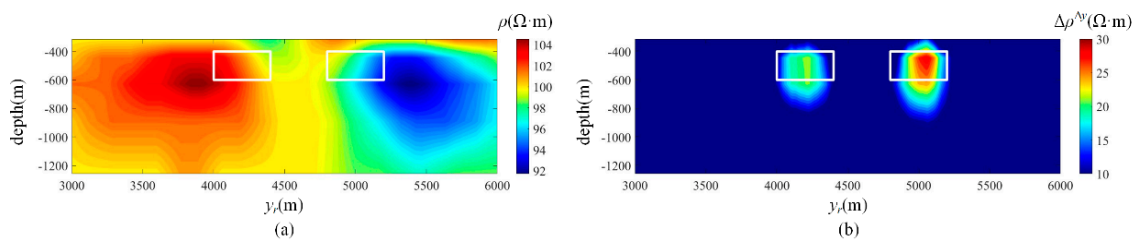


Figure 13. The imaging results for model III: (a) the apparent resistivity calculated from magnetic field, (b) the apparent resistivity variation predicted from magnetic field gradient $H_z^{\Delta y}$. The white boxes indicate the outlines of the conductive abnormal bodies.

The calculated results of the apparent resistivity obtained by the traditional iteration-matching procedure are shown in Figures 9a,c, 11a and 13a. As the magnetic field primarily reflects changes in subsurface electrical properties, the distribution of apparent resistivity derived from the magnetic field exhibits significant changes at anomaly boundaries, thereby limiting its ability to indicate the center of anomalies. In contrast, Figures 9b,d, 11b and 13b show the predicted results of the apparent resistivity variation by the NGO-LSSVM algorithm, which indicate the anomaly location clearly and demonstrate the feasibility of such predictions. Notably, since diffusion causes apparent resistivity to reach extreme values at boundaries, the largest variation in apparent resistivity occurs precisely at the center of anomalies. Consequently, utilizing magnetic field gradients to predict distributions of apparent resistivity variations enables more accurate identification of anomaly locations.

4. Field Data Example

In order to verify the reasonability of the proposed algorithm, a field test was conducted. The Chengba great fault is located in the Bashan-Chengkou-Fangxian area of the South Dabashan mountains, also known as the “Chengkou-Fangxian deep fault” or “Dabashan Mountain deep fault”. The northwestern terminus of the Chengba fault commences in Xixiang, Shaanxi province, intersecting with the Yangpingguan-Yangxian deep fault. On its eastern end, the Chengba fracture extends into Hubei province and intersects with the Xiangfan-Guangji fault within Fangxian county. The Chengba fault has a general arc distribution, and its distribution pattern is prominent to the southwest. Spanning over 300 km in length, this fault serves as a tectonic boundary between the Yangtze plate and the South Qinling plate.

In the Chengkou area, the Chengba fault zone exhibits a generally undulating plane, with the fault plane predominantly oriented due north, dipping at an angle between 40° and 80° . The layout of the electric source and test line are designed as shown in Figure 14. In the test, the transmitter equipment is the ground-airborne electromagnetic transmission system developed by Jilin University with a maximum transmitting power of 200 kW. The received part used an unmanned aerial vehicle to load the lightweight receiver system. The flight speed is about 6 m/s and, during the apparent resistivity imaging, we acquire a point every 2 s, so the station spacing is around 12 m, then we obtain data with a lateral resolution of 12 m after data processing. The margin of error in data interpretation does not exceed 5%.

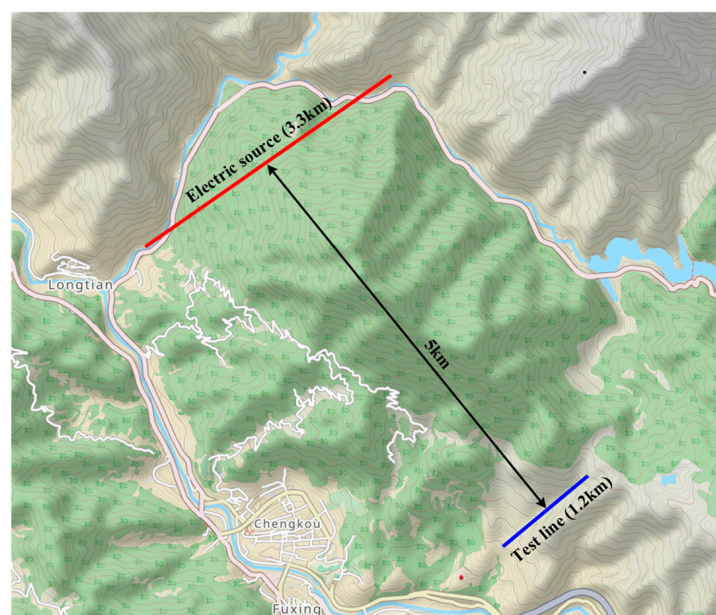


Figure 14. Layout of the source (in red) and the receiving positions (in blue).

The proposed NGO-LSSVM algorithm is used to interpret the measured data. According to the previous analysis, the variation in apparent resistivity of the conductive anomaly body is positive, indicating that as the resistivity decreases, the variation in apparent resistivity will reach a positive maximum value. The resistivity, however, exhibits a decrease in the presence of low resistance anomalies. Therefore, its trend of resistivity variation should be opposite to that of the resistivity. To compare the results of the apparent resistivity calculated from magnetic field and the apparent resistivity variation predicted from magnetic field gradient, Figure 15a shows the calculated apparent resistivity results, and Figure 15b is the predicted apparent resistivity variation results. The red lines indicate the inferred location of the Chengba fault zone, and the magenta line indicates the drill hole. In Figure 15a, the indication of the fault location is not clear enough in the apparent resistivity imaging section, so further analysis of the apparent resistivity-height curves at the sites is needed to identify the fault definitively [36]. However, in Figure 15b, the apparent resistivity variation imaging section reveals a distinct conductive area at the location of the fault, as depicted by the black dotted line, thereby enhancing the indication ability of the imaging sections. In addition, there is a suspected low-resistance region on the right side of the fault zone. To provide a clearer depiction of the distribution of apparent resistivity variation and facilitate a comparative analysis with the measuring of resistivity in the geological drilling method, Figure 16 illustrates the contrasting curves between the measured resistivity and predicted apparent resistivity variation at drill hole DW-01.

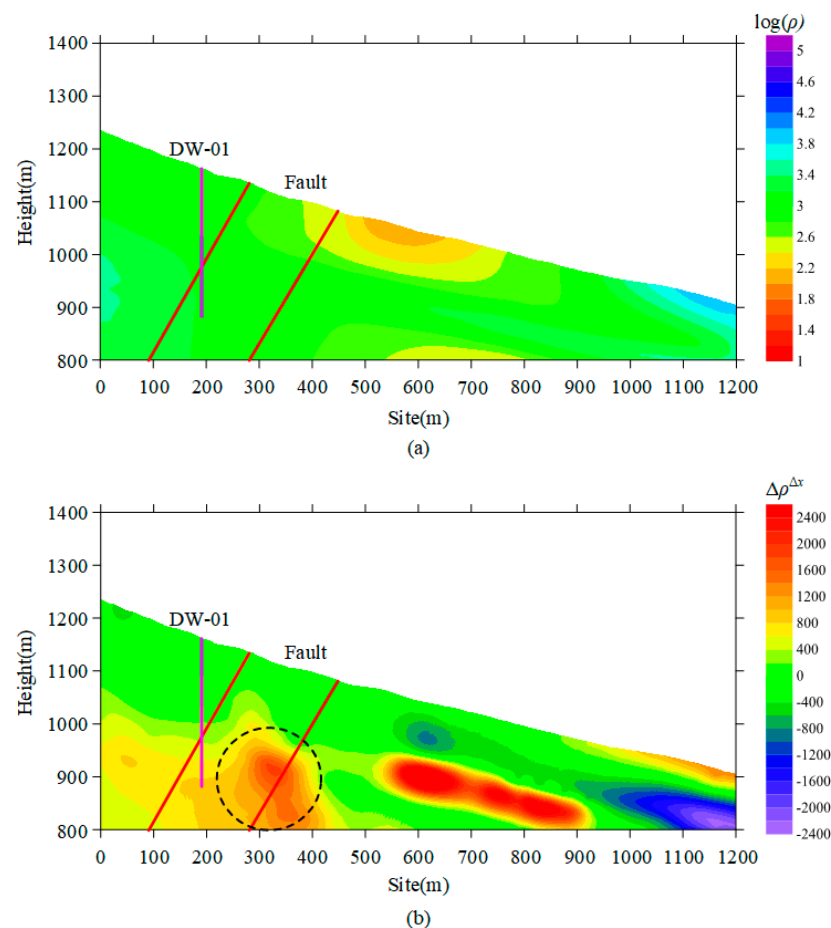


Figure 15. Comparison between apparent resistivity and apparent resistivity variation. (a) Apparent resistivity-depth section calculated from magnetic field H_z , (b) apparent resistivity variation-depth section predicted from magnetic field gradient $H_z^{\Delta x}$.

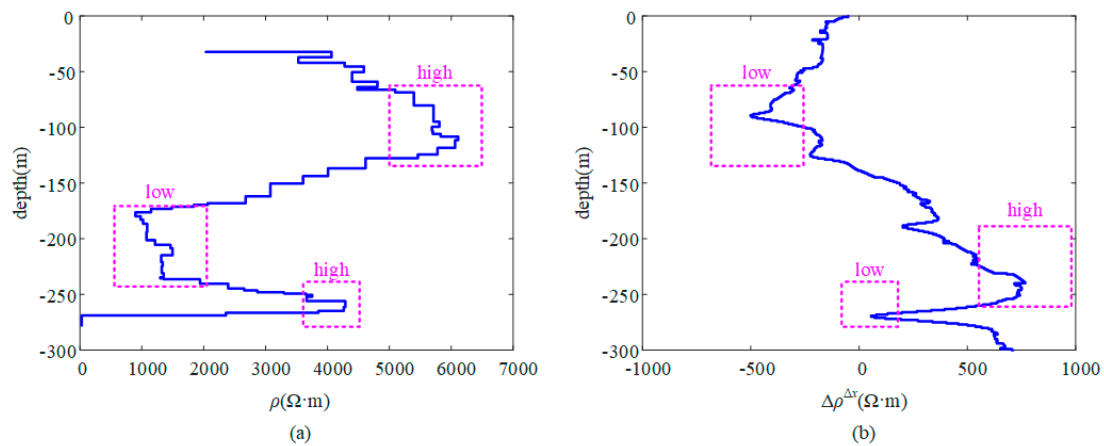


Figure 16. Comparison of resistivity from geological drilling method and predicted apparent resistivity variation by NGO-LSSVM algorithm: (a) resistivity curve of drill hole DW-01, (b) apparent resistivity variation curve of drill hole DW-01.

The measured resistivity curve at DW-01 by the geological drilling method is shown in Figure 16a, and the predicted resistivity variation curve by the NGO-LSSVM model is shown in Figure 16b. The resistivity value at a depth of -100 m in Figure 16a is high, corresponding to the low apparent resistivity variation value observed at the same depth in Figure 16b. The low resistivity value at a depth of -230 m corresponds to the high apparent resistivity variation value observed at the same depth. The high resistivity at a depth of -265 m corresponds to the low apparent resistivity variation value observed at the same depth in Figure 16b. Therefore, the predicted results of the apparent resistivity variation based on NGO-LSSVM can effectively indicate the fault zone location and accurately reflect the underground resistivity variation trend.

5. Conclusions

In order to convert the magnetic gradient data with high recognition ability to underground anomalies into electrical parameters for better data interpretation, the method of calculating the apparent resistivity variation from magnetic field gradient was studied in this paper. Firstly, we investigated the relationship between the magnetic field gradients and the earth's resistivity and found that each magnetic field gradient corresponds to a specific resistivity value at a certain measuring point, which enabled us to use the iteration-matching algorithm to solve the apparent resistivity. However, by calculating the apparent resistivity of uniform half-space models with different resistivities, it was found that random artificial anomalies exist, called background resistivity. Secondly, to mitigate the presence of random artificial anomalies, we employ LSSVM to obtain the apparent resistivity variation, eliminating the effect of background resistivity. Thirdly, to enhance the accuracy and avoid premature convergence to locally optimal solutions of LSSVM, the NGO algorithm was introduced to optimize the regularization parameter γ and the kernel parameter σ . Finally, to verify the predictive capability of the NGO-LSSVM algorithm, three theoretical models were designed. The apparent resistivity variation predicted from the magnetic field gradient by the NGO-LSSVM algorithm in this paper was significantly better than the apparent resistivity calculated from the traditional magnetic field; a field test was conducted, and the imaging results demonstrated a clear depiction of the Chengba fault zone through apparent resistivity variation, and the borehole resistivity variation was in good agreement with the measured results of the geological drilling method. Although the apparent resistivity variation calculated from magnetic field gradient through the NGO-LSSVM algorithm can indicate the location of the anomalous body, further research is essential to develop combined imaging with traditional apparent resistivity to obtain the apparent resistivity closer to the real situation. The range of underground electrical parameters can be initially obtained through the calculation results of traditional apparent

resistivity. Then, within this range of apparent resistivity, the design model is refined to enrich the amount of data involved in the training network of the apparent resistivity variation, so that the prediction results of the apparent resistivity variation are more reasonable, and more accurate apparent resistivity sections results can be obtained after combining with the apparent resistivity.

Author Contributions: Conceptualization, C.L. and J.L.; methodology, J.L.; software, J.L.; validation, J.L. and S.L.; resources, C.L. and H.Z.; data curation, H.Z.; writing—original draft preparation, J.L.; writing—review and editing, C.L., J.L., S.L. and H.Z.; visualization, J.L. and S.L.; supervision, H.Z.; project administration, C.L.; funding acquisition, C.L. and H.Z. All authors have read and agreed to the published version of the manuscript.

Funding: This research was funded by the Science and Technology Project of Jilin Department (grant number 20220201102GX) and the National Natural Science Foundation of China (grant number 42074152).

Institutional Review Board Statement: Not applicable.

Informed Consent Statement: Not applicable.

Data Availability Statement: The raw data supporting the conclusions of this article will be made available by the authors on request.

Acknowledgments: We thank all members in the EM group of the Key Lab of Geo-Exploration Instrumentation, Ministry of Education of China, who provided assistance for the field test.

Conflicts of Interest: The authors declare no conflicts of interest.

References

1. Steuer, A.; Smirnova, M.; Becken, M.; Schiffler, M.; Günther, T.; Rochlitz, R.; Yogeshwar, P.; Mörbe, W.; Siemon, B.; Costabel, S.; et al. Comparison of Novel Semi-Airborne Electromagnetic Data with Multi-Scale Geophysical, Petrophysical and Geological Data from Schleiz, Germany. *J. Appl. Geophys.* **2020**, *182*, 104172. [[CrossRef](#)]
2. Lin, J.; Kang, L.; Liu, C.; Ren, T.; Zhou, H.; Yao, Y.; Yu, S.; Liu, T.; Liu, P.; Zhang, M. The Frequency-Domain Airborne Electromagnetic Method with a Grounded Electrical Source. *Geophysics* **2019**, *84*, E269–E280. [[CrossRef](#)]
3. Becken, M.; Nittinger, C.G.; Smirnova, M.; Steuer, A.; Martin, T.; Petersen, H.; Meyer, U.; Mörbe, W.; Yogeshwar, P.; Tezkan, B.; et al. DESMEX: A Novel System Development for Semi-Airborne Electromagnetic Exploration. *Geophysics* **2020**, *85*, E253–E267. [[CrossRef](#)]
4. Smirnova, M.V.; Becken, M.; Nittinger, C.; Yogeshwar, P.; Mörbe, W.; Rochlitz, R.; Steuer, A.; Costabel, S.; Smirnov, M.Y.; the DESMEX Working Group. A Novel Semiairborne Frequency-Domain Controlled-Source Electromagnetic System: Three-Dimensional Inversion of Semiairborne Data from the Flight Experiment over an Ancient Mining Area near Schleiz, Germany. *Geophysics* **2019**, *84*, E281–E292. [[CrossRef](#)]
5. Nazari, S.; Rochlitz, R.; Günther, T. Optimizing Semi-Airborne Electromagnetic Survey Design for Mineral Exploration. *Minerals* **2023**, *13*, 796. [[CrossRef](#)]
6. Plessix, R.-É.; Mulder, W.A. Resistivity Imaging with Controlled-Source Electromagnetic Data: Depth and Data Weighting. *Inverse Probl.* **2008**, *24*, 034012. [[CrossRef](#)]
7. Liu, X.; Wang, Y. An Improved Conjugate Gradient Image Reconstruction Algorithm for Electromagnetic Tomography. *Sens Imaging* **2022**, *23*, 5. [[CrossRef](#)]
8. Qin, Y.; Li, K.; Yao, C.; Wang, X.; Ouyang, J.; Yang, X. Magnetic Anomaly Detection Using Full Magnetic Gradient Orthonormal Basis Function. *IEEE Sens. J.* **2020**, *20*, 12928–12940. [[CrossRef](#)]
9. Liu, C.; Liu, S.; Li, Z.; Wang, L.; Kan, S.; Liang, J. Research on Ground-Airborne Frequency-Domain Electromagnetic Rapid Imaging Method Based on Space Magnetic Gradient Anomaly. *IEEE Trans. Geosci. Remote Sens.* **2023**, *61*, 5910810. [[CrossRef](#)]
10. Zhang, M.; Farquharson, C.G.; Liu, C. Improved Controlled Source Audio-frequency Magnetotelluric Method Apparent Resistivity Pseudo-sections Based on the Frequency and Frequency-Spatial Gradients of Electromagnetic Fields. *Geophys. Prospect.* **2021**, *69*, 474–490. [[CrossRef](#)]
11. Sarker, I.H. Machine Learning: Algorithms, Real-World Applications and Research Directions. *SN Comput. Sci.* **2021**, *2*, 160. [[CrossRef](#)]
12. Alzubi, J.; Nayyar, A.; Kumar, A. Machine Learning from Theory to Algorithms: An Overview. *J. Phys. Conf. Ser.* **2018**, *1142*, 012012. [[CrossRef](#)]
13. Qiu, J.; Wu, Q.; Ding, G.; Xu, Y.; Feng, S. A Survey of Machine Learning for Big Data Processing. *Eurasip J. Adv. Signal Process.* **2016**, *2016*, 67. [[CrossRef](#)]

14. Hansen, T.M.; Finlay, C.C. Use of Machine Learning to Estimate Statistics of the Posterior Distribution in Probabilistic Inverse Problems—An Application to Airborne EM Data. *JGR Solid Earth* **2022**, *127*, e2022JB024703. [[CrossRef](#)]
15. Jordan, M.I.; Mitchell, T.M. Machine Learning: Trends, Perspectives, and Prospects. *Science* **2015**, *349*, 255–260. [[CrossRef](#)]
16. Zhang, L.; Poulton, M.M.; Wang, T. Borehole Electrical Resistivity Modeling Using Neural Networks. *Geophysics* **2002**, *67*, 1790–1797. [[CrossRef](#)]
17. Taylor, C.L.; Vasco, D.W. Inversion of Gravity Gradiometry Data Using a Neural Network. In *SEG Technical Program Expanded Abstracts 1990*; Society of Exploration Geophysicists: Houston, TX, USA, 1990; pp. 591–593.
18. Calderón-Macías, C.; Sen, M.K.; Stoffa, P.L. Artificial Neural Networks for Parameter Estimation in Geophysics. *Geophys. Prospect.* **2000**, *48*, 21–47. [[CrossRef](#)]
19. Chen, J.; Zhang, Y.; Lin, T. Transient Electromagnetic Machine Learning Inversion Based on Pseudo Wave Field Data. *IEEE Trans. Geosci. Remote Sens.* **2022**, *60*, 5917410. [[CrossRef](#)]
20. Vapnik, V.N. An Overview of Statistical Learning Theory. *IEEE Trans. Neural Netw.* **1999**, *10*, 988–999. [[CrossRef](#)]
21. Ghezlbash, R.; Maghsoudi, A.; Carranza, E.J.M. Performance Evaluation of RBF- and SVM-Based Machine Learning Algorithms for Predictive Mineral Prospectivity Modeling: Integration of S-A Multifractal Model and Mineralization Controls. *Earth Sci. Inform.* **2019**, *12*, 277–293. [[CrossRef](#)]
22. Liang, X.; Qi, T.; Jin, Z.; Qian, W. Hybrid Support Vector Machine Optimization Model for Inversion of Tunnel Transient Electromagnetic Method. *Math. Biosci. Eng.* **2020**, *17*, 3998–4017. [[CrossRef](#)] [[PubMed](#)]
23. Zhong, Y.; Li, R. Application of principle component analysis and least square support vector machine to lithology identification. *Well Logging Technol.* **2009**, *33*, 425–429.
24. Li, M.; Li, Y.; Wu, N.; Tian, Y.; Wang, T. Desert Seismic Random Noise Reduction Framework Based on Improved PSO–SVM. *Acta Geod. Geophys.* **2020**, *55*, 101–117. [[CrossRef](#)]
25. Suykens, J.A.K.; Vandewalle, J.; De Moor, B. Optimal Control by Least Squares Support Vector Machines. *Neural Netw.* **2001**, *14*, 23–35. [[CrossRef](#)] [[PubMed](#)]
26. Suykens, J.A.K.; Vandewalle, J. Least Squares Support Vector Machine Classifiers. *Neural Process. Lett.* **1999**, *9*, 293–300. [[CrossRef](#)]
27. Xue, X. Prediction of Slope Stability Based on Hybrid PSO and LSSVM. *J. Comput. Civ. Eng.* **2017**, *31*, 04016041. [[CrossRef](#)]
28. Kadkhodazadeh, M.; Farzin, S. A Novel LSSVM Model Integrated with GBO Algorithm to Assessment of Water Quality Parameters. *Water Resour. Manag.* **2021**, *35*, 3939–3968. [[CrossRef](#)]
29. Baziyad, A.G.; Nouh, A.S.; Ahmad, I.; Alkuhayli, A. Application of Least-Squares Support-Vector Machine Based on Hysteresis Operators and Particle Swarm Optimization for Modeling and Control of Hysteresis in Piezoelectric Actuators. *Actuators* **2022**, *11*, 217. [[CrossRef](#)]
30. Dehghani, M.; Hubalovsky, S.; Trojovsky, P. Northern Goshawk Optimization: A New Swarm-Based Algorithm for Solving Optimization Problems. *IEEE Access* **2021**, *9*, 162059–162080. [[CrossRef](#)]
31. Yu, S.; Ma, J. Adaptive Composite Fault Diagnosis of Rolling Bearings Based on the CLNGO Algorithm. *Processes* **2022**, *10*, 2532. [[CrossRef](#)]
32. Liang, Y.; Hu, X.; Hu, G.; Dou, W. An Enhanced Northern Goshawk Optimization Algorithm and Its Application in Practical Optimization Problems. *Mathematics* **2022**, *10*, 4383. [[CrossRef](#)]
33. Zhong, J.; Chen, T.; Yi, L. Face Expression Recognition Based on NGO-BILSTM Model. *Front. Neurobot.* **2023**, *17*, 1155038. [[CrossRef](#)] [[PubMed](#)]
34. Espinoza, M.; Suykens, J.A.K.; Moor, B.D. Fixed-Size Least Squares Support Vector Machines: A Large Scale Application in Electrical Load Forecasting. *Comput. Manag. Sci.* **2006**, *3*, 113–129. [[CrossRef](#)]
35. Mercer, J. Functions of Positive and Negative Type, and Their Connection with the Theory of Integral Equations. *Philos. Trans. R. Soc. Lond.* **1909**, *209*, 415–446.
36. Liu, C.; Liang, J.; Kang, N.; Li, Z. Sensitive Characteristics of Contributed Region and Detectability Analysis for Semi-Airborne Frequency-Domain Electromagnetic System. *J. Appl. Geophys.* **2023**, *215*, 105116. [[CrossRef](#)]

Disclaimer/Publisher’s Note: The statements, opinions and data contained in all publications are solely those of the individual author(s) and contributor(s) and not of MDPI and/or the editor(s). MDPI and/or the editor(s) disclaim responsibility for any injury to people or property resulting from any ideas, methods, instructions or products referred to in the content.